Supplement of Nat. Hazards Earth Syst. Sci., 26, 1835–1857, 2026
https://doi.org/10.5194/nhess-26-1835-2026-supplement

Natural Hazards and Earth System Sciences
Open Access
EGU

Supplement of

Leveraging reforecasts for flood estimation with long continuous simulation: a proof-of-concept study

Daniel Viviroli et al.

Correspondence to: Daniel Viviroli (daniel.viviroli@geo.uzh.ch)

S1 Feasibility of dynamical downscaling

Statistical and dynamical downscaling provide complementary approaches to generating high-resolution precipitation data. Statistical downscaling, as applied in this study, is computationally efficient but has limitations in representing small-scale convective extremes. Dynamical downscaling, in contrast, explicitly resolves physical processes and provides spatio-temporally consistent results, making it particularly relevant for small-scale convective precipitation events. However, its high computational cost restricts its applicability for exceedingly long datasets such as the nearly 10 000 years of RF data considered here, which would require pre-selection of extreme events for dynamical downscaling.

We tested the feasibility of dynamically downscaling the ECMWF RFs to the convection-permitting scale (~3 km grid spacing), which would improve the representation of short local extreme precipitation events and be valuable for small catchments. To model rapid regional weather changes such as those associated with small-scale extreme events, the raw data (in our case RFs) should be available at high temporal resolution. Typically, these data (e.g., reanalyses or data from global climate models) are stored every 6 or 3 hours and must be interpolated to the required temporal resolution. The ECMWF RFs we used were stored at 6-hour resolution for the first two forecast weeks, but only at 12-hour resolution for the extended range beyond day 15. This raised the concern that short-term extreme events lasting only a few hours would not be captured. This risk arises due to the methodology of dynamical downscaling: the limited-area regional model requires atmospheric driving data at each model time step (20 seconds) along its lateral boundaries. These driving data are linearly interpolated in time from the available RF data. Hence, if the RF data are available only at 12-hour resolution, processes beyond this resolution are poorly resolved, although the regional model is partially capable of reintroducing sub-daily processes.

We therefore tested whether dynamical downscaling driven by 12-hourly input data could reproduce the local extreme events produced when hourly input data were used. Since the RF data are only available at a coarse temporal resolution, ERA5 reanalysis data (Hersbach et al., 2020) with a grid spacing of 25 km and a temporal resolution of 1 hour were used as a surrogate to test the sensitivity to input temporal resolution. The ECMWF forecast model underlying ERA5 is very similar to that used for the RFs. Dynamical downscaling was performed with the CCLM model (Rockel et al., 2008; Schättler et al., 2021).

The two extreme events of 8 July 1996 and 23 June 2021 were considered. While the simulations driven by 1-hourly input produced realistic results, simulations driven at 12-hour intervals showed a marked reduction in simulated extreme precipitation and spatial distortions in the precipitation field. As a result, extreme events driven by fast convective processes may be substantially underestimated or lost entirely.

In summary, it was not possible to identify the relevant extreme events for dynamical downscaling because the link between the scales was not pronounced enough, especially with the limited 12-hour resolution available. Higher temporal and spatial resolution of ECMWF RF data would be required to reliably identify relatively small-scale extreme precipitation events for catchments of approximately 500 km^2 or smaller. While dynamical downscaling remains suitable for large-scale extreme events, it offers no clear advantage over stochastic downscaling at these scales. In the future, dynamical downscaling could substantially improve the representation of short-duration convective events, provided that RF data become available at a higher temporal resolution.

S2 Supplementary figures

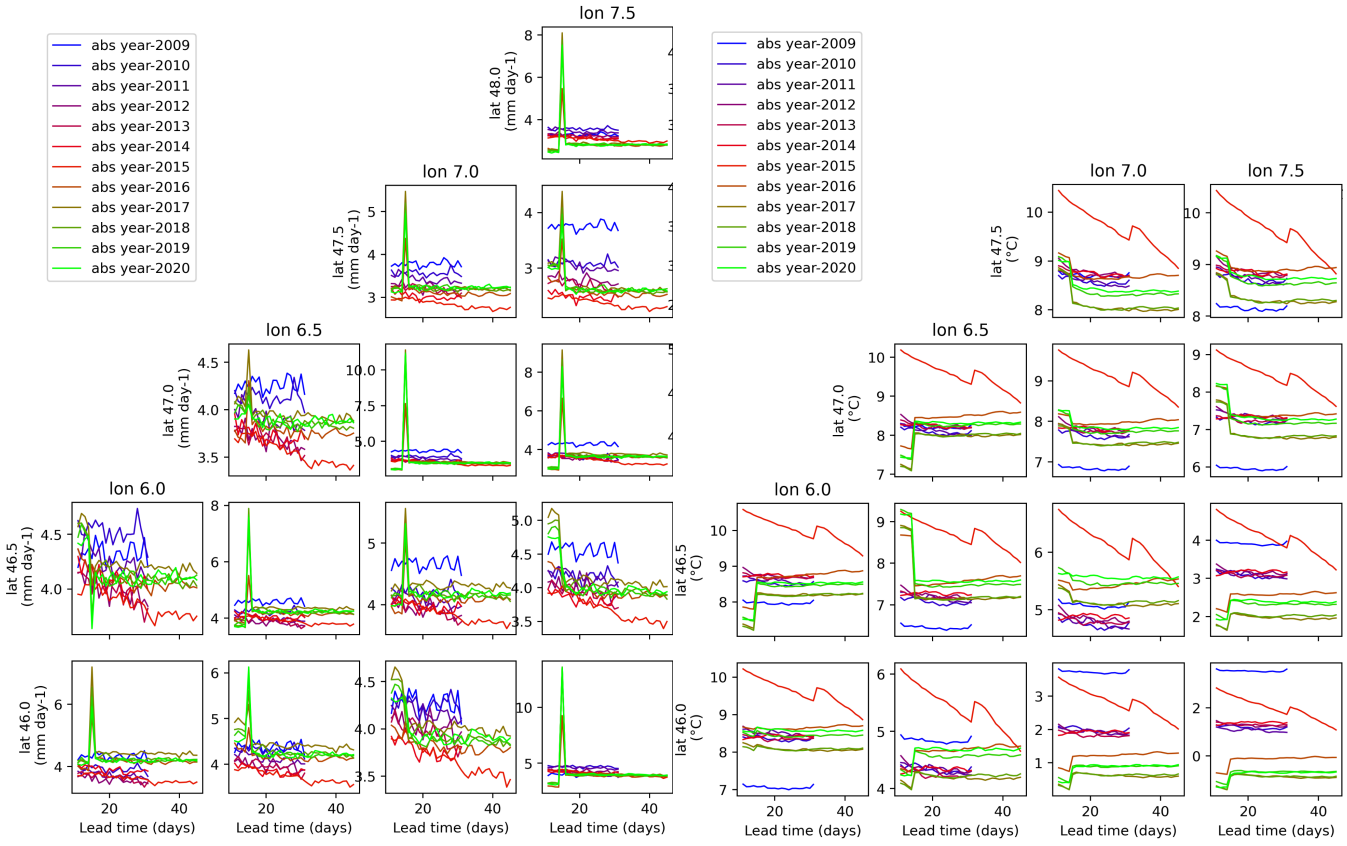

Figure S1. Annual mean ECMWF reforecast precipitation (left) and temperature (right) for selected grid points over Switzerland, plotted by forecast time (days 11 to 45) and by initialization year.

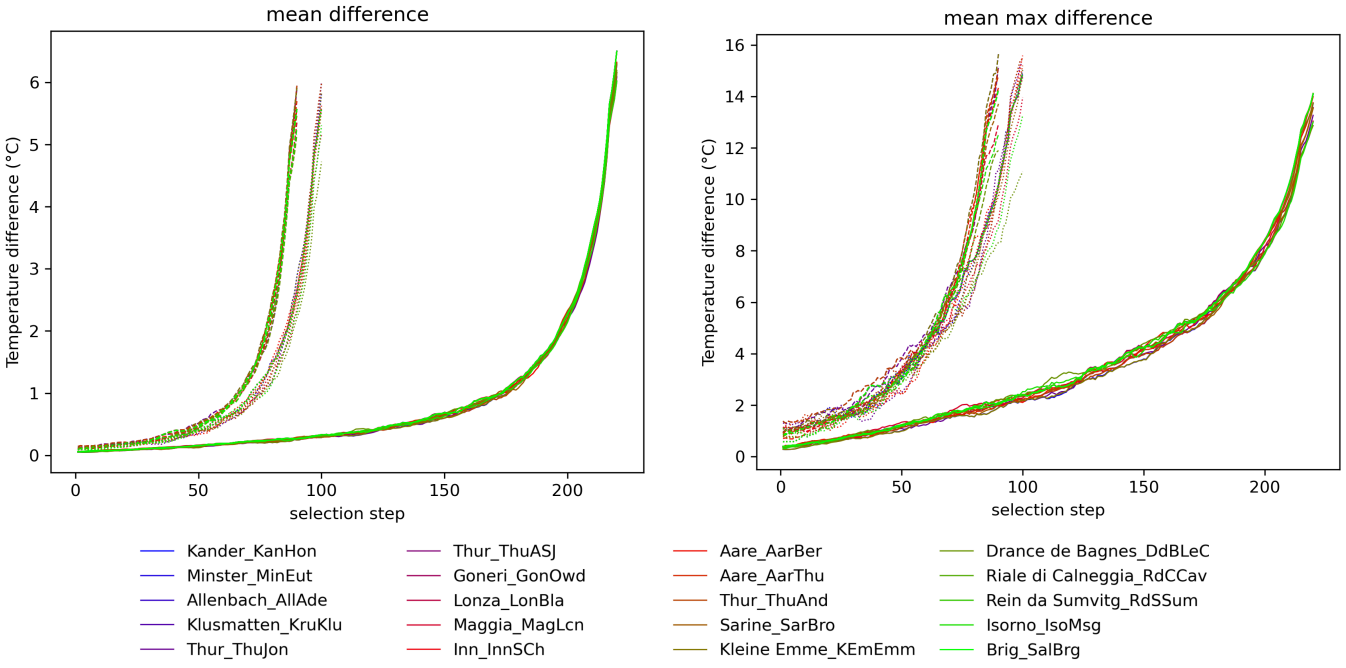

Figure S2. Mean (left) and maximum (right) 6-hourly raw temperature difference at the intersection time of concatenated single ECMWF RFs. Dashed lines are for RFs initialized between 2009–2012, dotted lines for RFs initialized between 2013–2014, and solid lines for RFs initialized between 2016–2020. A running mean of 11 selection steps was applied.

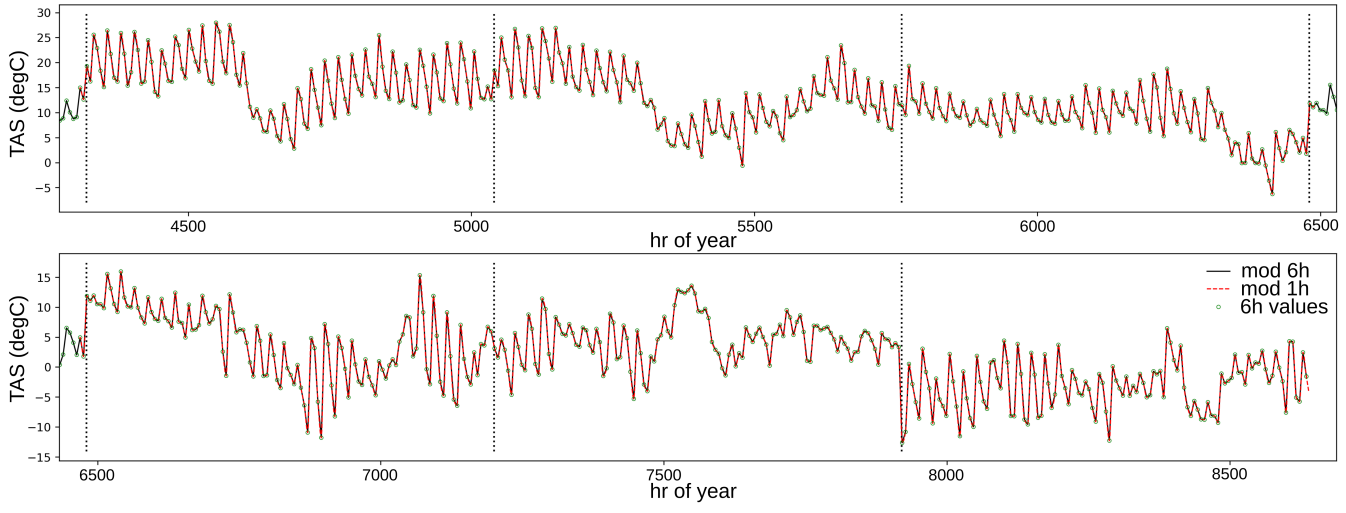

Figure S3. Time series of temperature (TAS) for the second half-year of an example year (year 9920) with an extreme temperature jump at the station Adelboden (ABO) in the Kander River catchment (at approximately hour 7900). The stitching points between single reforecasts are indicated by vertical dotted lines.

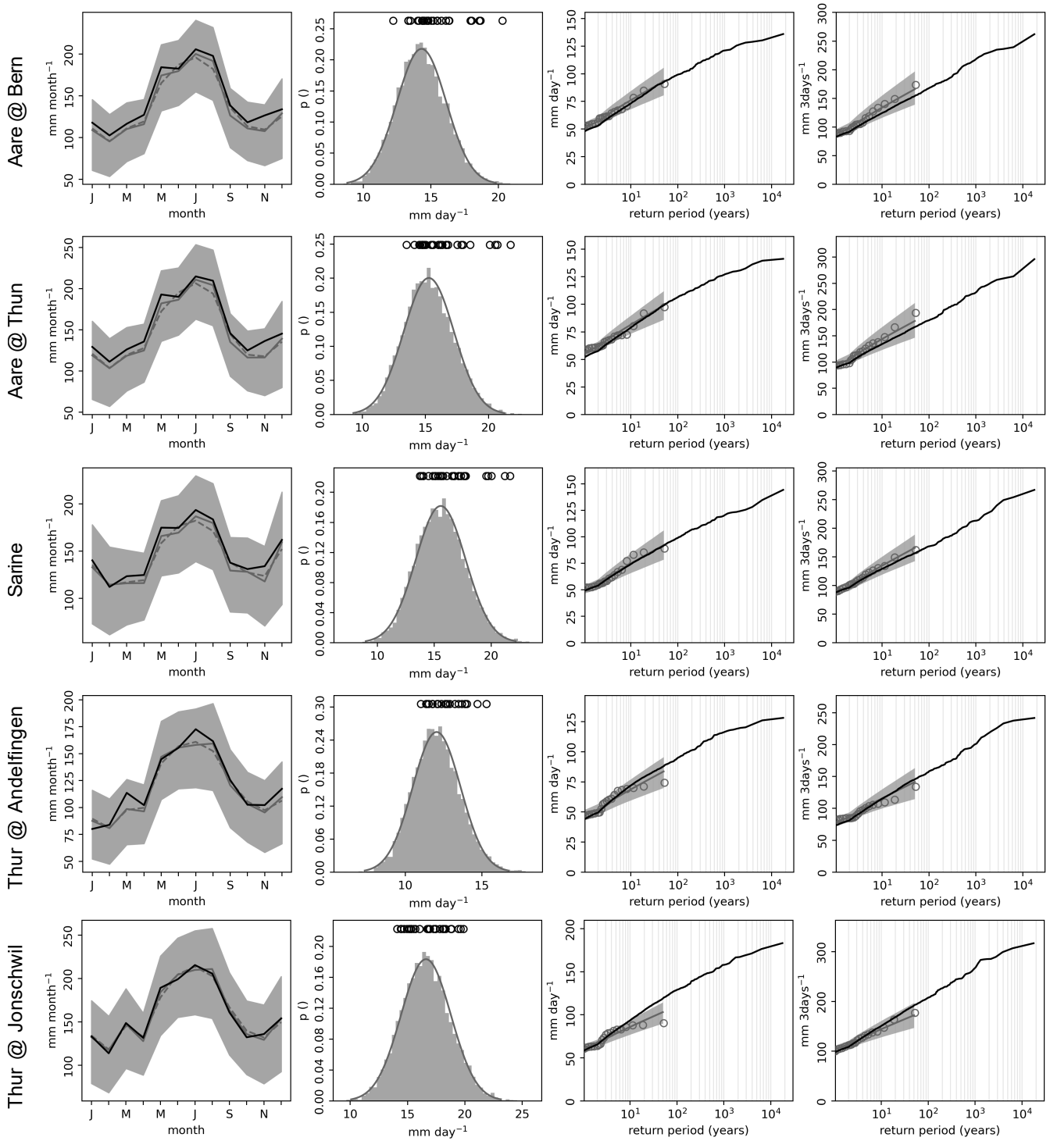

Figure S4. Evaluation of reforecast (RF) precipitation for large catchments: Aare at Bern, Aare at Thun, Sarine, Thur at Andelfingen, Thur at Jonschwil. From left to right: Annual cycle of mean monthly precipitation for observations (1991–2019, black) and RF (grey, shading p25–p75; dashed line based on 360-day calendar); histogram of annual daily p90 precipitation for RF, and observations (black circles); return levels for annual maximum daily and maximum 3-day precipitation for RF (black) and observation (grey circles) using the Gringorten plotting position. For observations, return values have additionally been fitted using a Gumbel distribution (using a GEV distribution resulted in overly broad confidence intervals) and maximum likelihood estimates, confidence intervals are based on 5000 bootstrap samples (mean in dark grey, p2.5–97.5 grey shading).

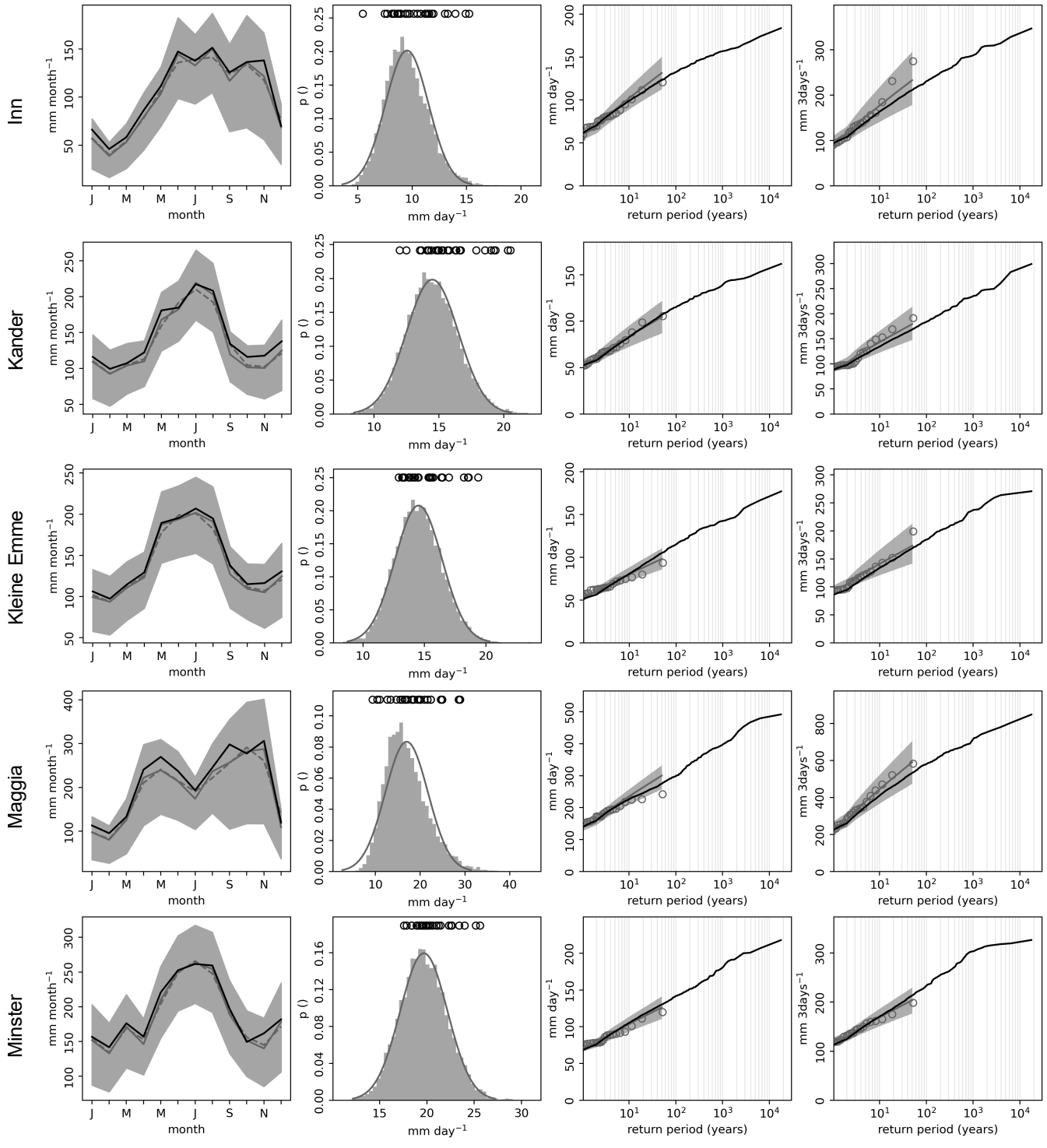

Figure S5. Same as Fig. S4, but for medium-sized catchments: Inn, Kander, Kleine Emme, Maggia, and Minster.

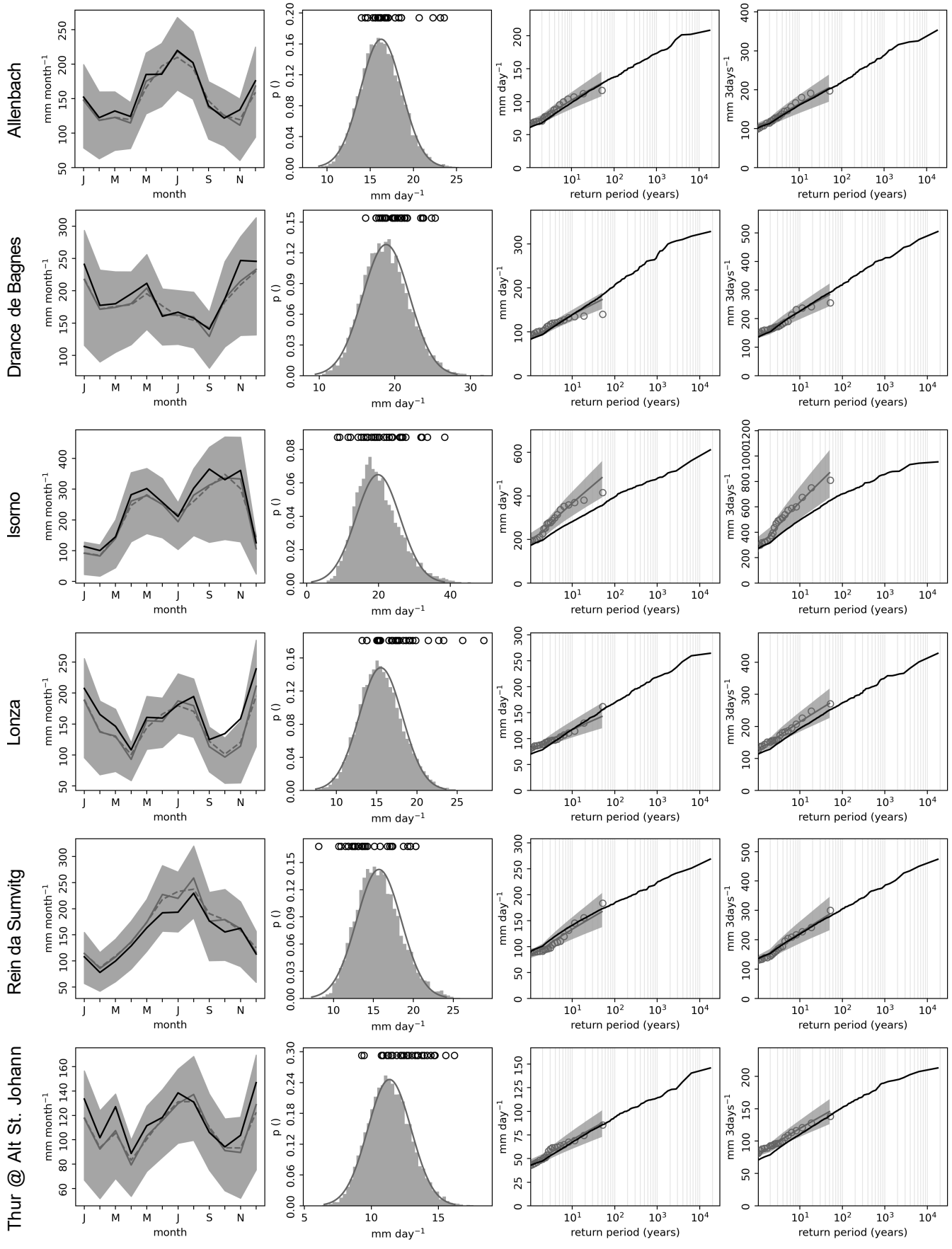

Figure S6. Same as Fig. S4, but for small catchments: Allenbach, Drance de Bagnes, Isorno, Lonza, Rein da Sumvitg and Thur at Alt St. Johann.

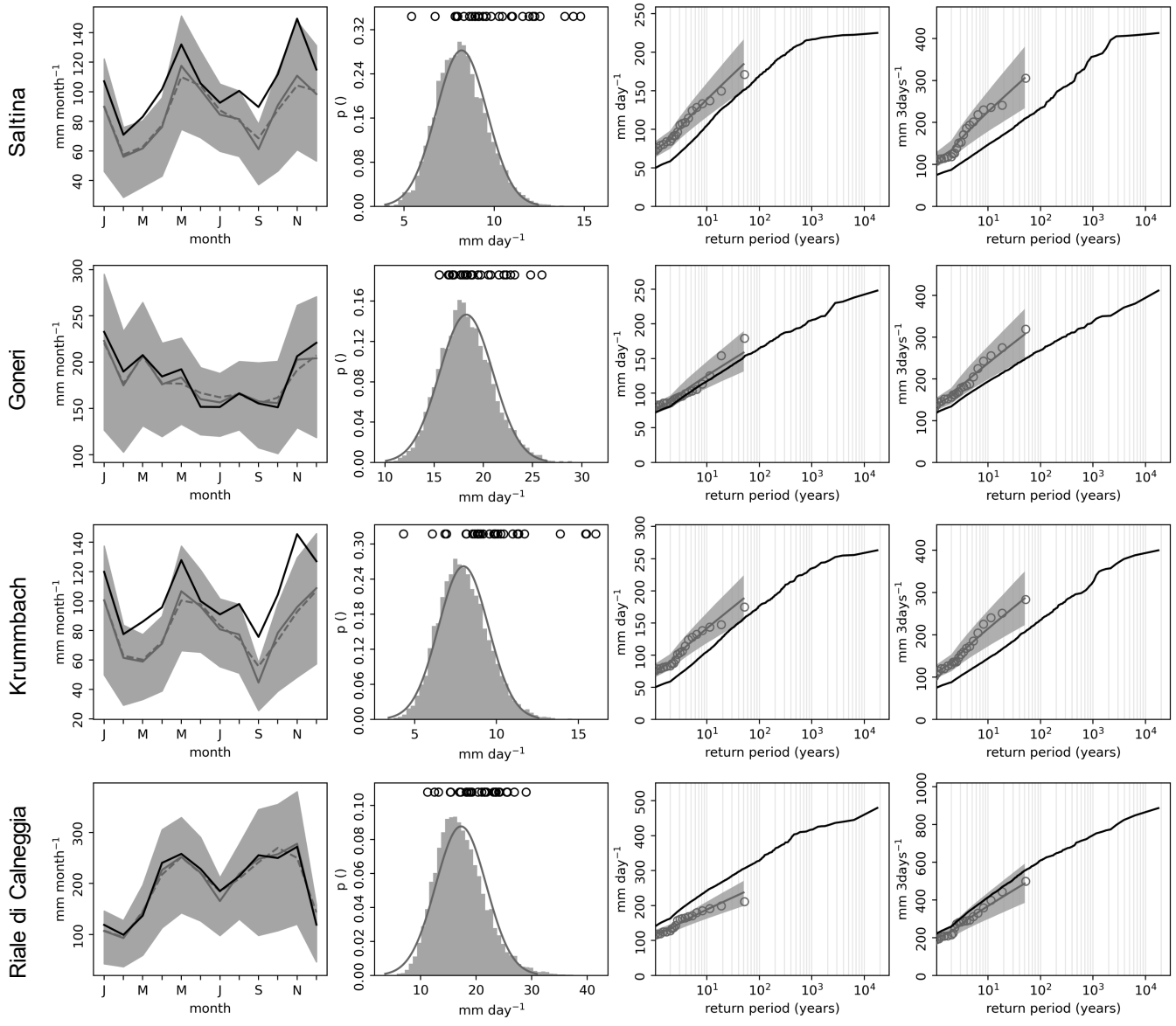

Figure S7. Same as Fig. S4, but for very small catchments: Saltina, Goneri, Krummbach and Riale di Calneggia.

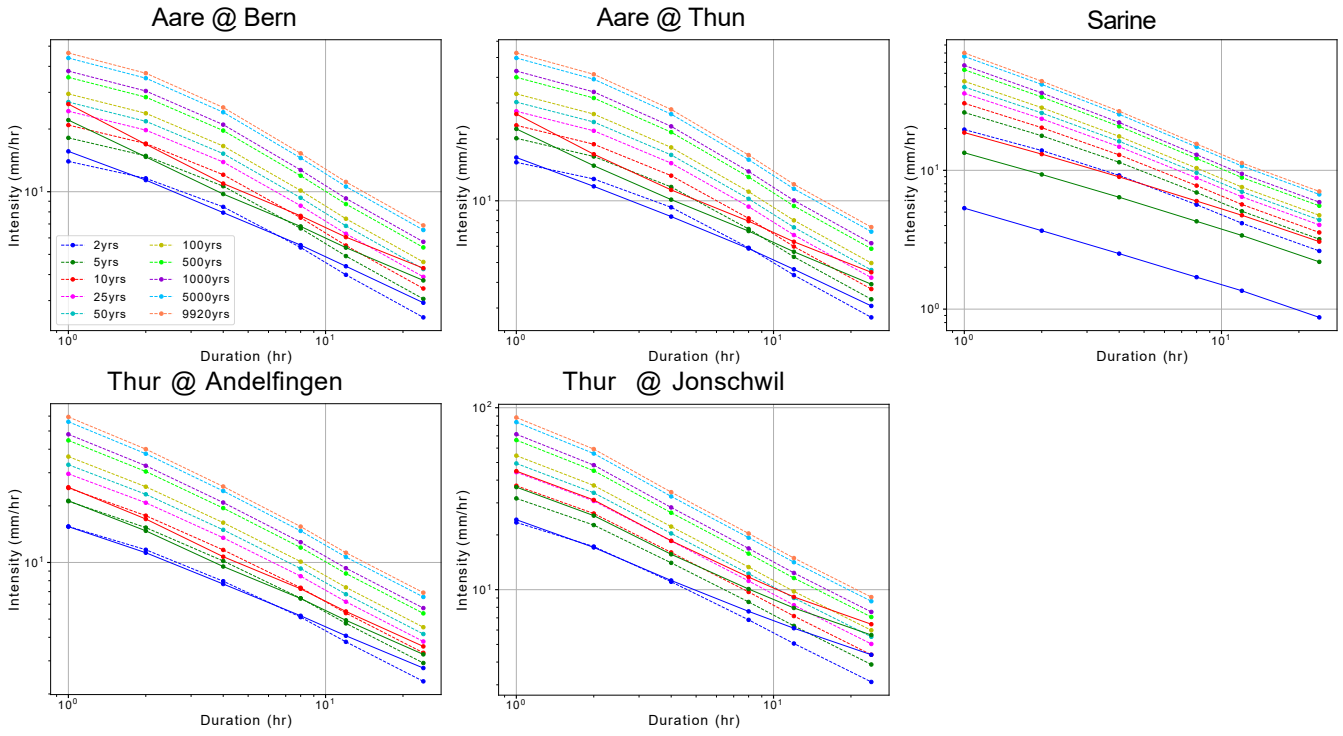

Figure S8. Average intensity-duration-frequency (IDF) curves (1h to 24h) for different return periods (colors) in large catchments: Aare at Bern, Aare at Thun, Sarine, Thur at Andelfingen and Thur at Jonschwil. Reforecast results are shown with dashed lines, observations spanning 1981–2019 and used for the analog method are shown with solid lines. The IDFs have been derived using the Gumbel method (Ponce, 1989), and a 360-day calendar was used.

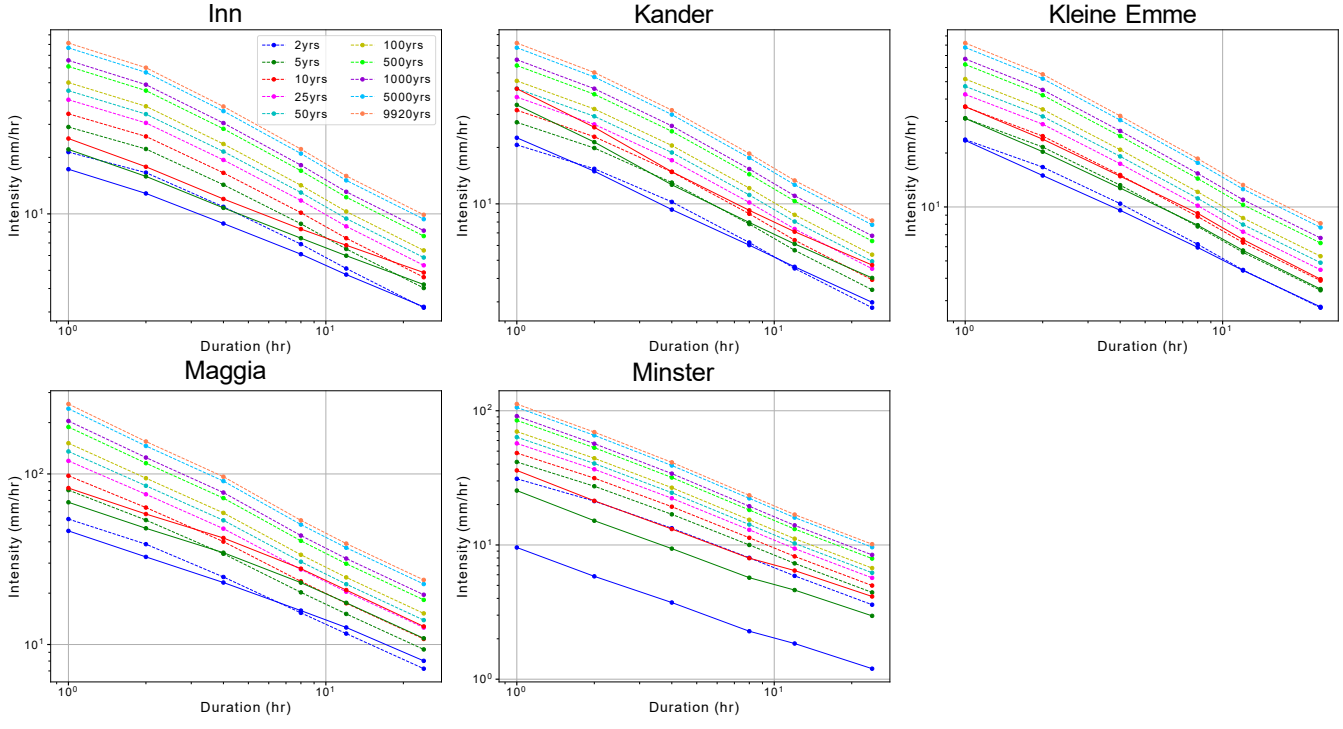

Figure S9. Same as Fig. S8 but for medium-sized catchments: Inn, Kander, Kleine Emme, Maggia and Minster.

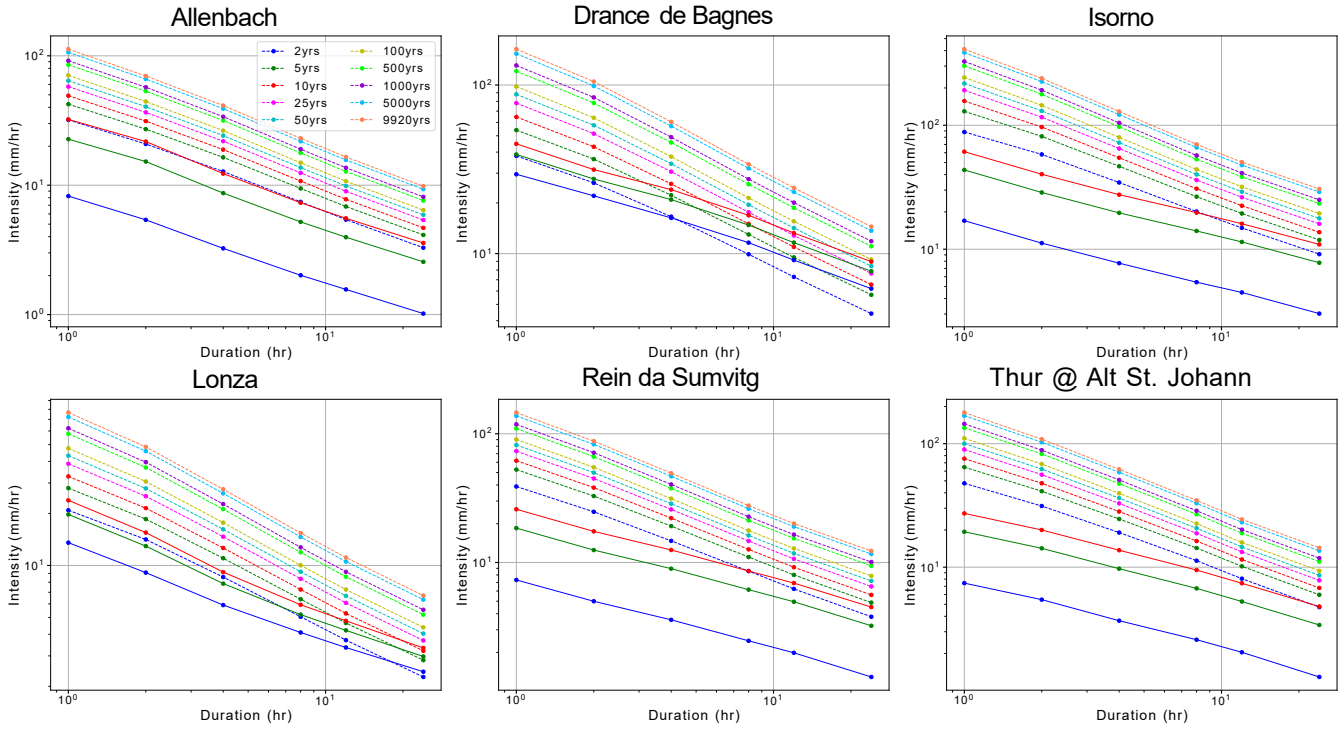

Figure S10. Same as Fig. S8 but for small catchments: Allenbach, Drance de Bagnes, Isorno, Lonza, Rein da Sumvitg and Thur at Alt St. Johann.

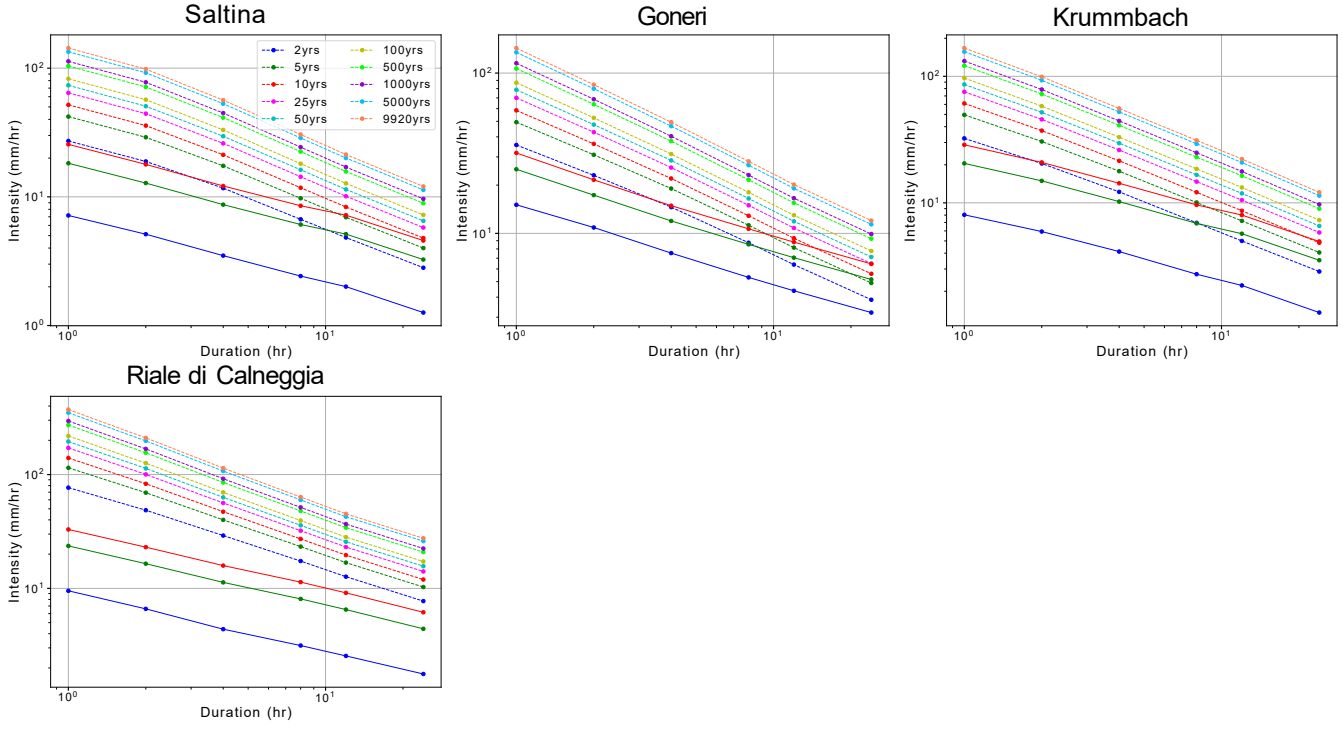

Figure S11. Same as Fig. S8 but for very small catchments: Saltina, Goneri, Krummbach and Riale di Calneggia.

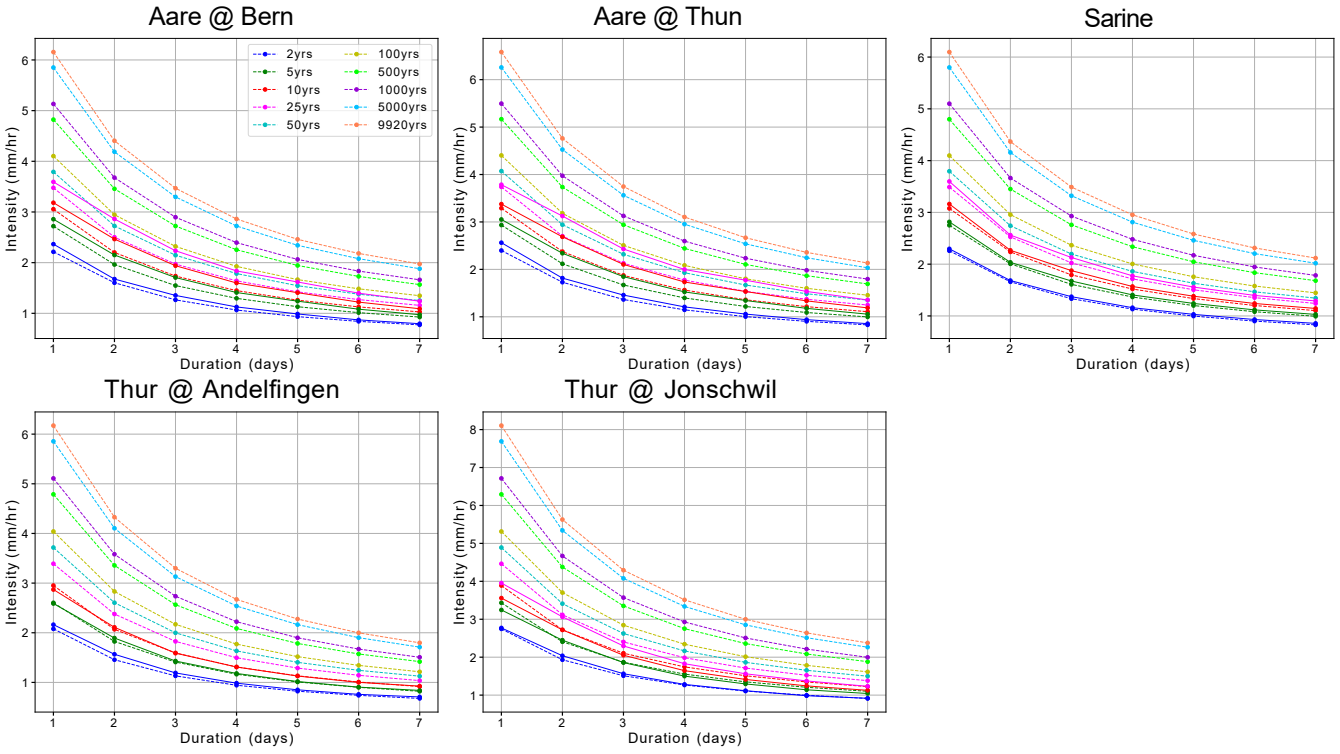

Figure S12. Average intensity-duration-frequency (IDF) curves (1-day to 7-day) for different return periods (colors) in large catchments: Aare at Bern, Aare at Thun, Sarine, Thur at Andelfingen and Thur at Jonschwil. Reforecast results are shown with dashed lines, observations spanning 1981–2019 and used for the analog method are shown with solid lines. The IDFs have been derived using the Gumbel method (Ponce, 1989), and a 360-day calendar was used.

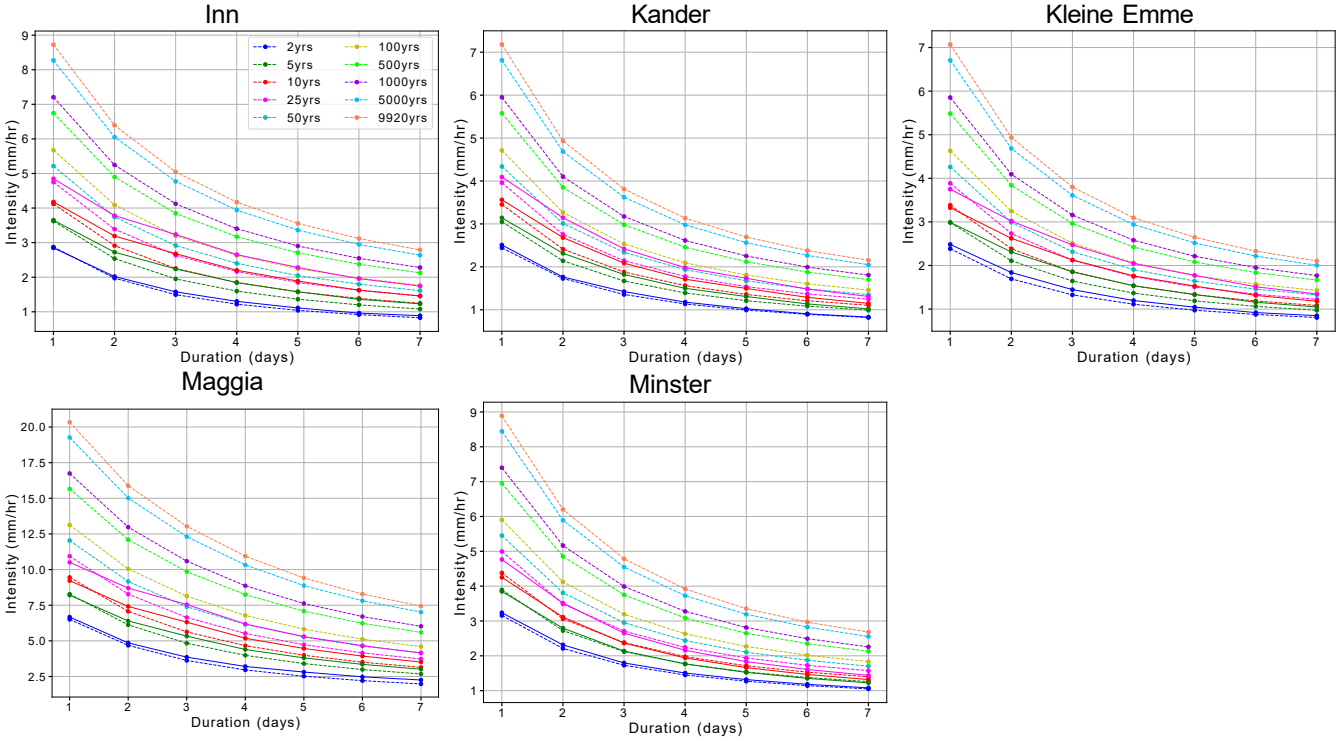

Figure S13. Same as Fig. S12 but for medium-sized catchments: Inn, Kander, Kleine Emme, Maggia and Minster.

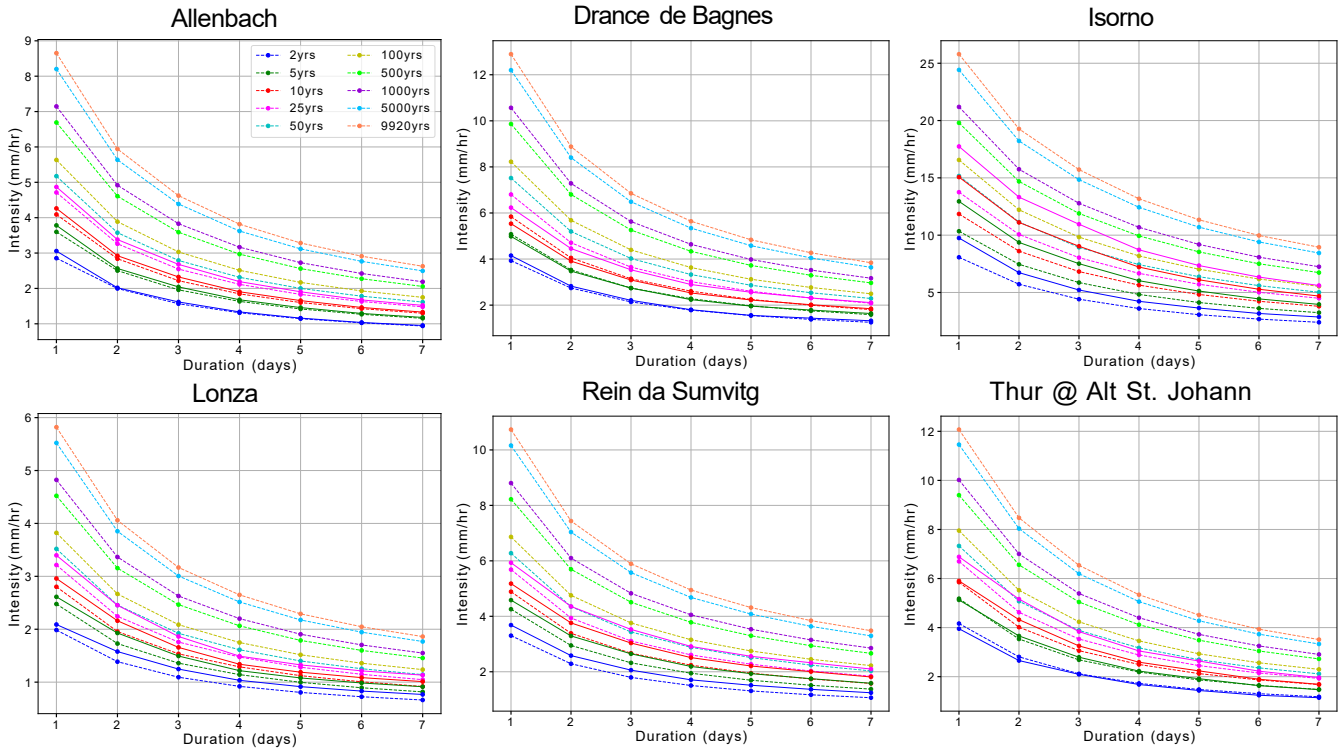

Figure S14. Same as Fig. S12 but for small catchments: Allenbach, Drance de Bagnes, Isorno, Lonza, Rein da Sumvitg and Thur at Alt St. Johann.

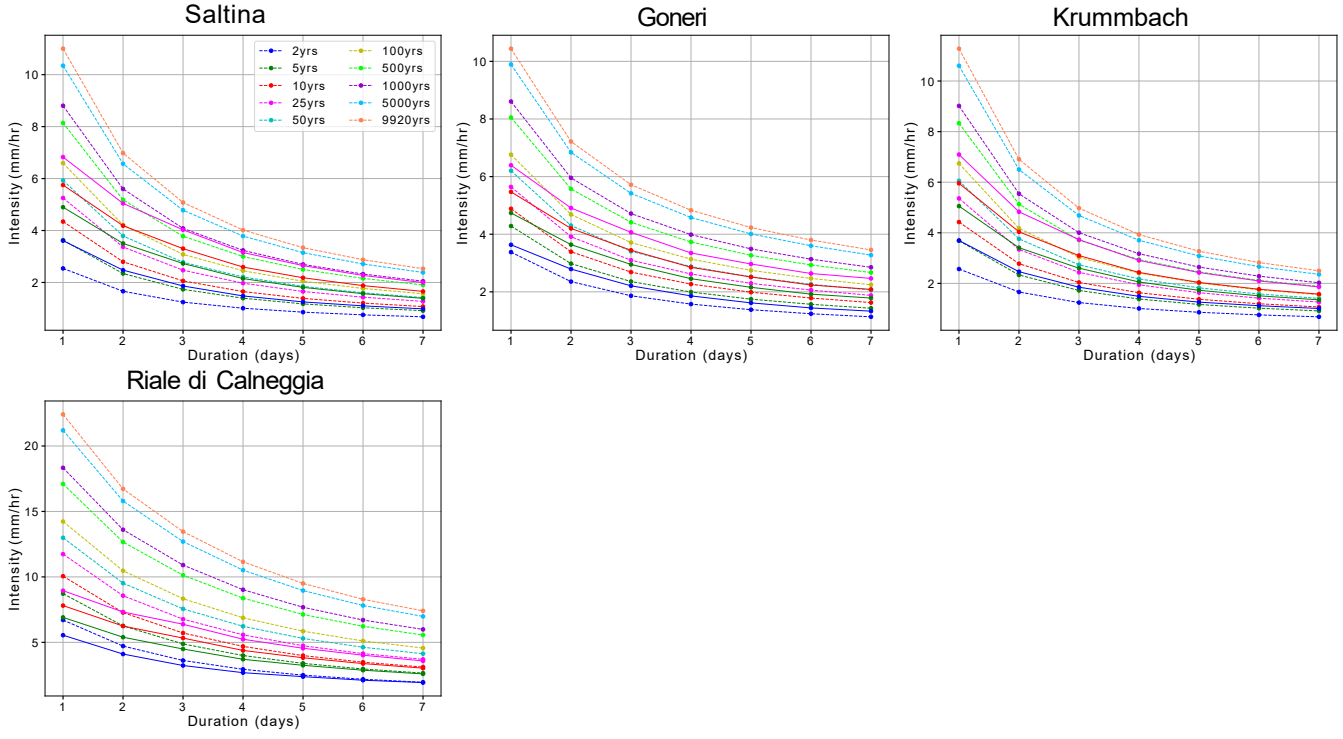

Figure S15. Same as Fig. S12 but for very small catchments: Saltina, Goneri, Krummbach and Riale di Calneggia.

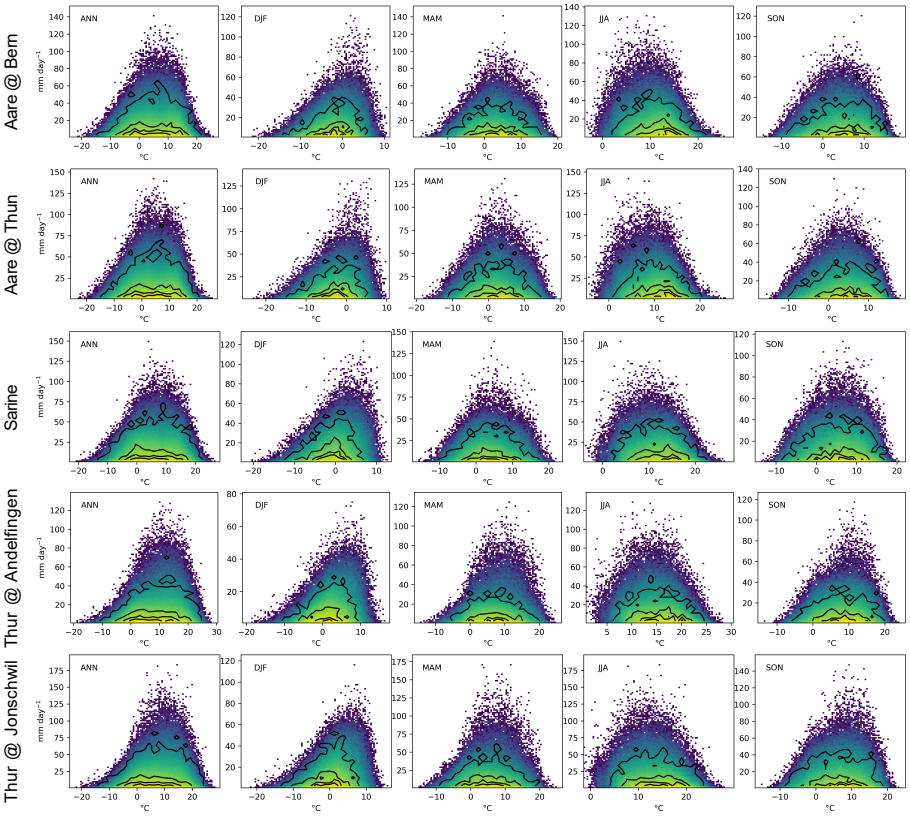

Figure S16. Annual and seasonal density plots based on daily mean temperature and precipitation ($\geq$1 mm day^{-1}) and the final 360-day calendar for large catchments. Colours range from blue for low density to yellow for high density. Observations over the 1991–2019 period are denoted by contour lines.

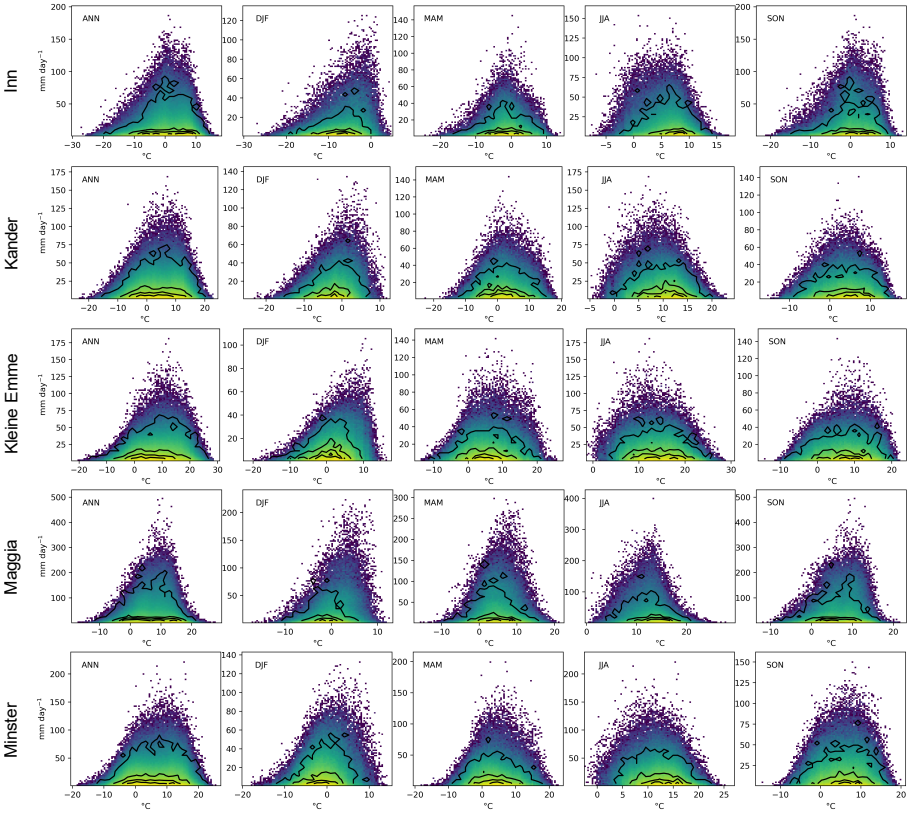

Figure S17. Same as Fig. S16, but for medium-sized catchments.

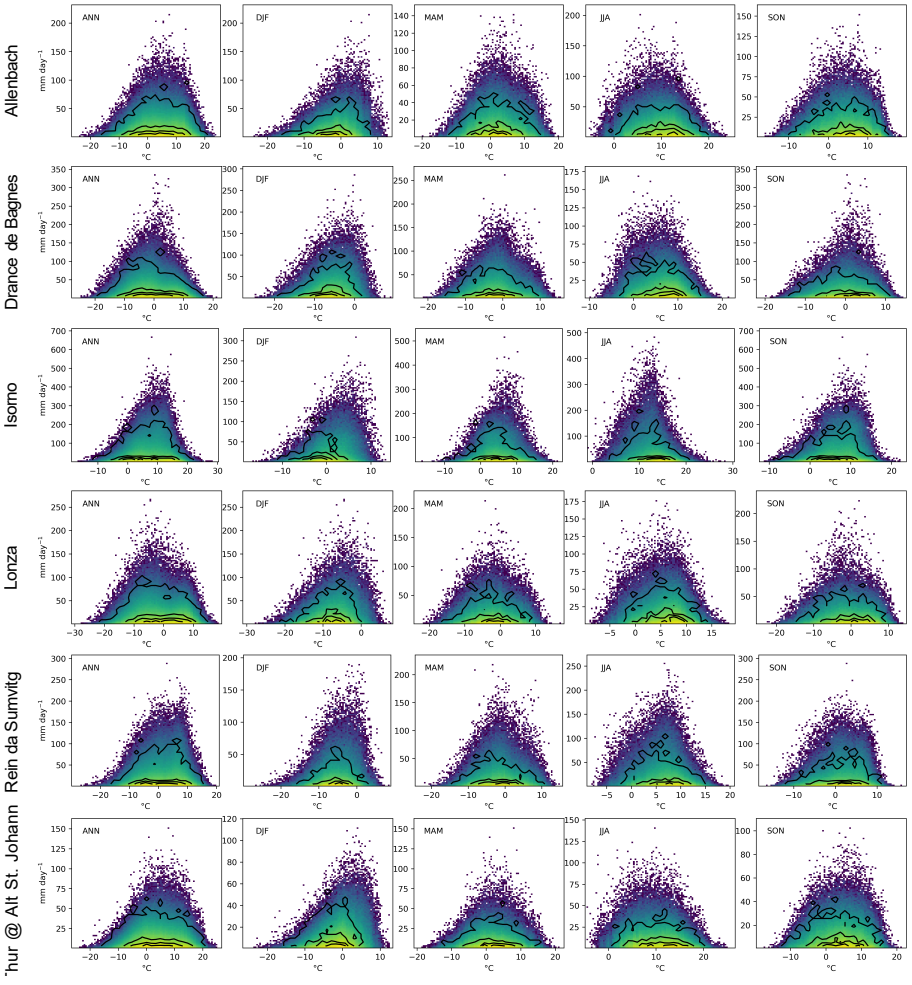

Figure S18. Same as Fig. S16, but for small catchments.

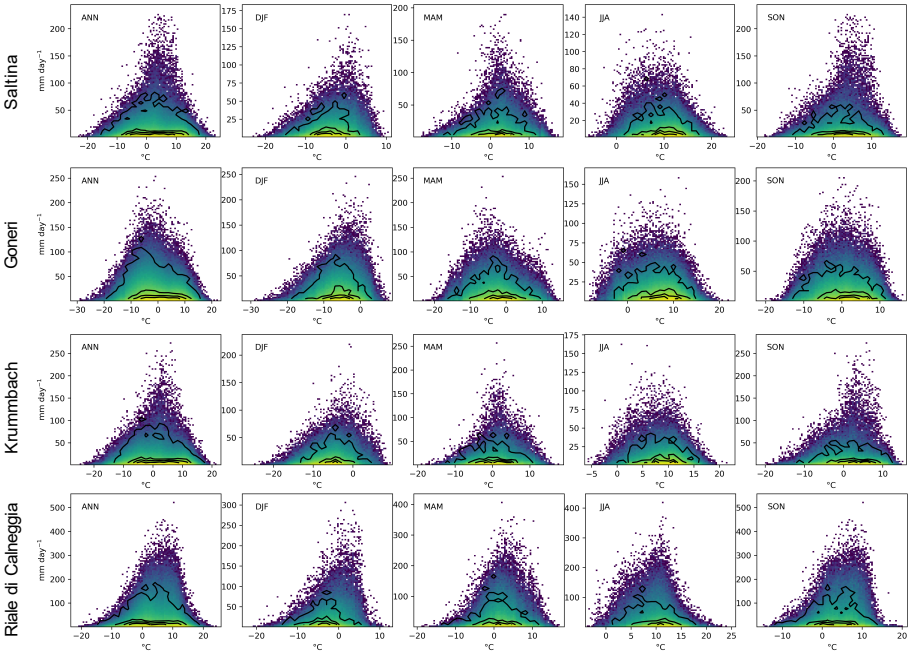

Figure S19. Same as Fig. S16, but for very small catchments.

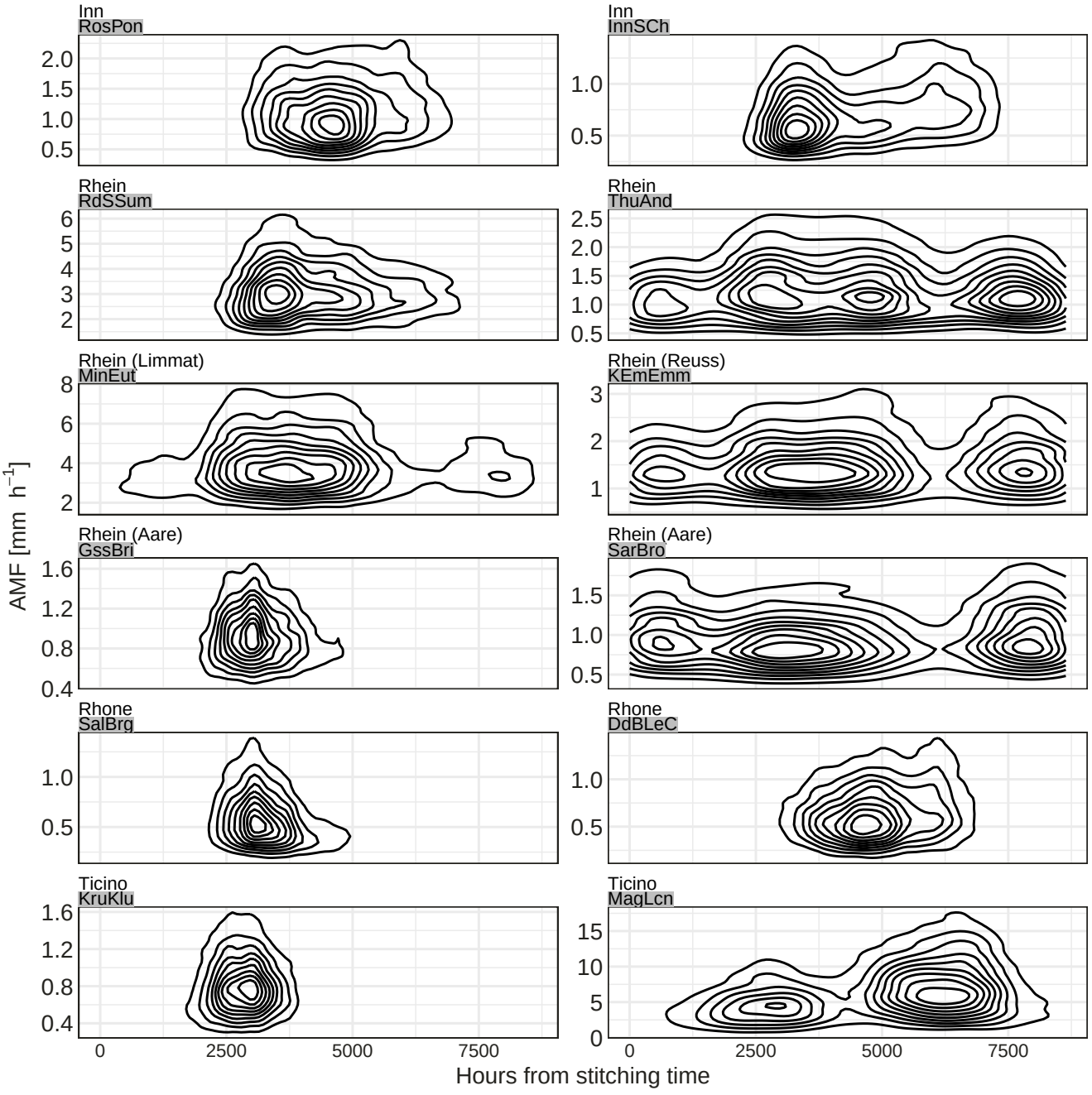

Figure S20. Contour density plots showing the magnitude of simulated annual maximum floods as a function of their occurrence time relative to the stitching points of individual RFs. Where available, both a smaller and a larger catchment were selected for each river basin.

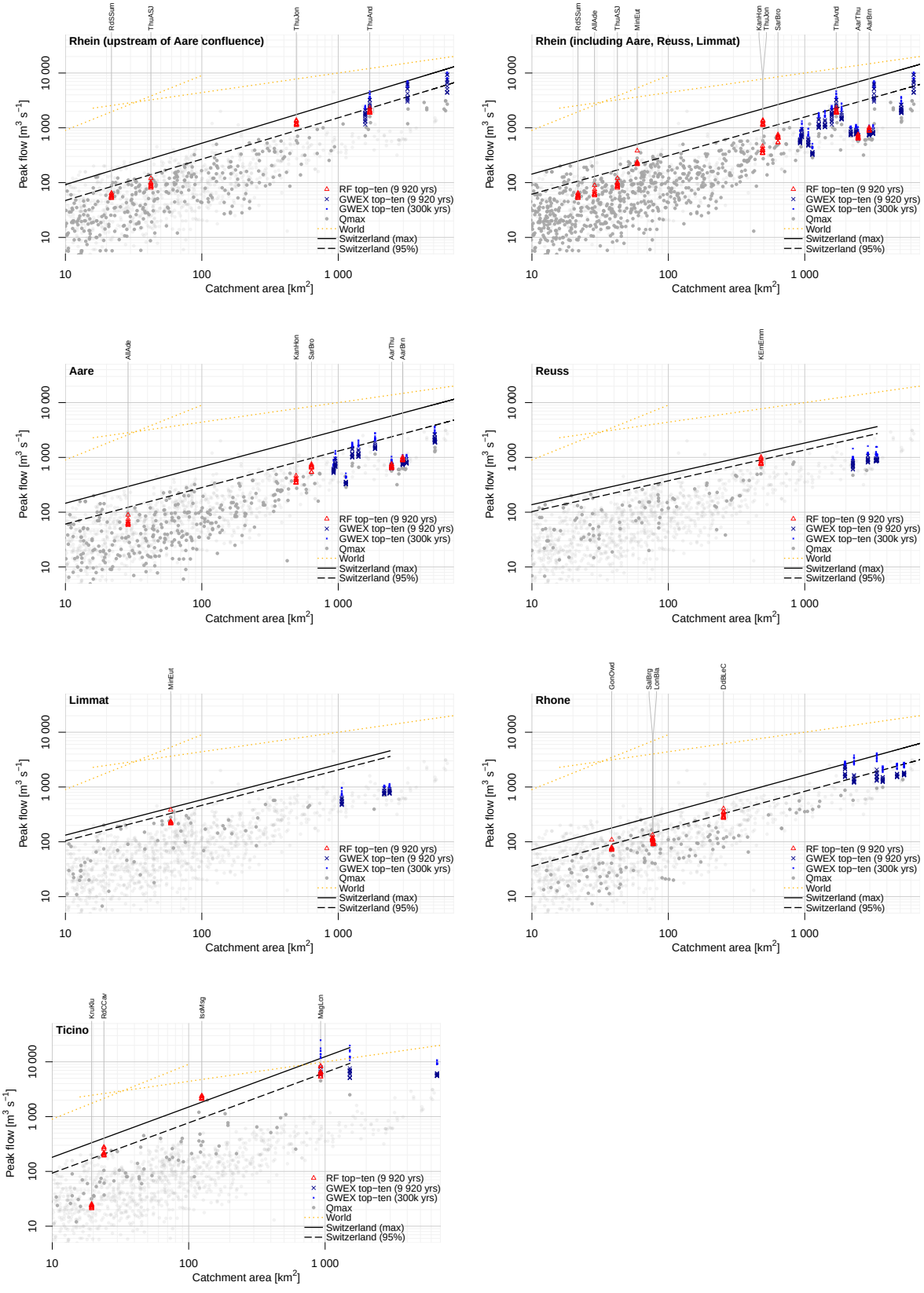

Figure S21. Highest ten annual maximum floods simulated using reforecast (RF) and weather generator (GWEX) input, presented separately for large river basins. Maximum observed floods in the corresponding large river basin (dark grey) and Switzerland (light grey) as per Kienzler and Scherrer (2018) (grey dots) are shown for context, along with an envelope curve for the corresponding large river basin (solid line: all data; dashed line: 95th percentile). Also shown is the envelope curve for maximum floods worldwide (Herschy, 2003). For catchment IDs see Table 1.

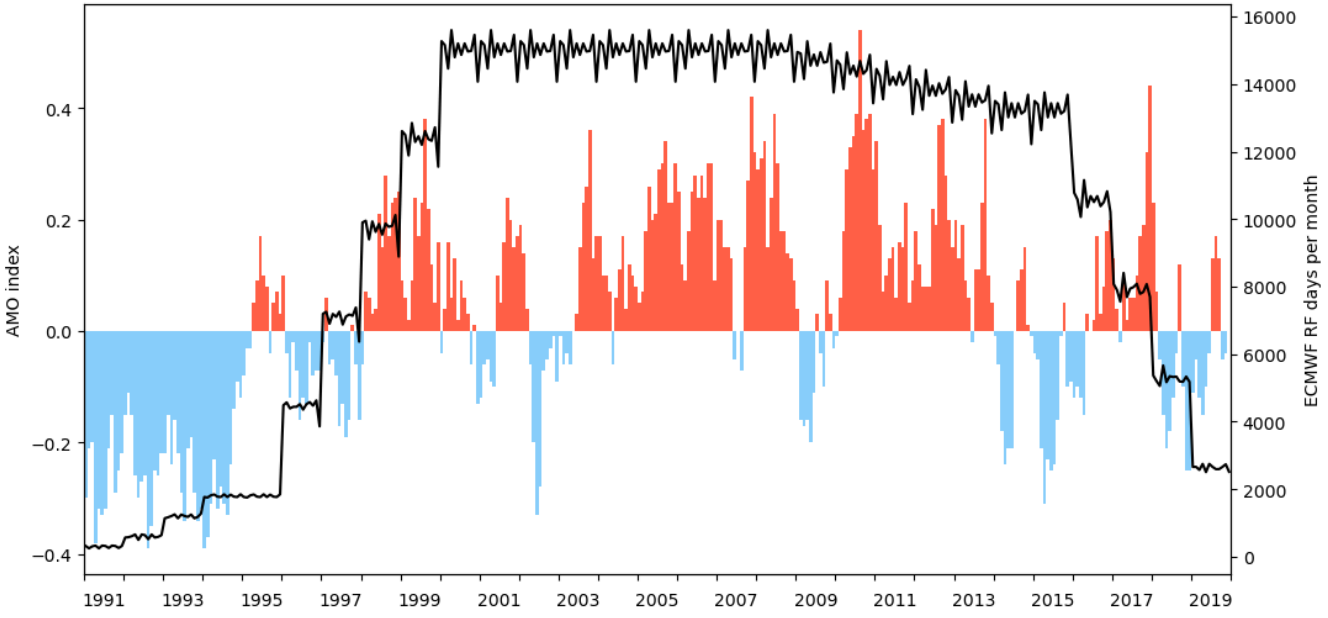

Figure S22. The Atlantic Multidecadal Oscillation (AMO) index compared with the total days of the sampled reforecasts within the 9920 RF years processed. The AMO data were obtained from NCAR and are based on Trenberth and Shea (2006) and HadISST1 (NCAR, 2023).

References

Hersbach, H., Bell, B., Berrisford, P., Hirahara, S., Horányi, A., Muñoz-Sabater, J., Nicolas, J., Peubey, C., Radu, R., Schepers, D., Simmons, A., Soci, C., Abdalla, S., Abellan, X., Balsamo, G., Bechtold, P., Biavati, G., Bidlot, J., Bonavita, M., de Chiara, G., Dahlgren, P., Dee, D., Diamantakis, M., Dragani, R., Flemming, J., Forbes, R., Fuentes, M., Geer, A., Haimberger, L., Healy, S., Hogan, R. J., Hólm, E., Janisková, M., Keeley, S., Laloyaux, P., Lopez, P., Lupu, C., Radnoti, G., de Rosnay, P., Rozum, I., Vamborg, F., Villaume, S., and Thépaut, J.-N.: The ERA5 global reanalysis, Quarterly Journal of the Royal Meteorological Society, 146, 1999–2049, https://doi.org/10.1002/qj.3803, 2020.

Herschy, R. W.: World Catalogue of Maximum Observed Floods, vol. 284 of *IAHS publication*, IAHS Press, Wallingford, ISBN 1-901502-47-3, 2003.

Kienzler, P. M. and Scherrer, S.: Verzeichnis grosser Hochwasserabflüsse in Schweizerischen Einzugsgebieten: Auswertung und graphische Aufbereitung, Reinach, https://www.bafu.admin.ch/bafu/de/home/themen/wasser/zustand/wasser--methoden/grosse_hochwasserabflusse-2.html, 2018.

NCAR: AMO Index Data provided by the Climate Analysis Section, NCAR, Boulder, USA, https://climatedataguide.ucar.edu/sites/default/files/2022-03/amo_monthly.txt, 2023.

Ponce, V. M.: Engineering Hydrology: Principles and Practices, Prentice Hall, ISBN 978-0133154665, 1989.

Rockel, B., Will, A., and Hense, A.: The Regional Climate Model COSMO-CLM (CCLM), Meteorologische Zeitschrift, 17, 347–348, https://doi.org/10.1127/0941-2948/2008/0309, 2008.

Schättler, U., Doms, G., and Schraff, C.: COSMO-Model Version 6.00: A Description of the Nonhydrostatic Regional COSMO-Model - Part VII: User's Guide, https://doi.org/10.5676/DWD_PUB/NWV/COSMO-DOC_6.00_VII, 2021.

Trenberth, K. E. and Shea, D. J.: Atlantic hurricanes and natural variability in 2005, Geophysical Research Letters, 33, https://doi.org/10.1029/2006GL026894, 2006.